AN INTEGRATED NEOTECTONIC STUDY OF THE ÇANAKLI BASIN (SW TURKEY): REMOTE SENSING, SURFACE GEOLOGY AND NEAR-SURFACE GEOPHYSICS

Dominique SIMILOX-TOHON, Max FERNANDEZ-ALONSO, Kris VANNESTE, Marc WAELKENS, Philippe MUCHEZ and Manuel SINTUBIN

1. INTRODUCTION

Archaeological evidence (Waelkens *et al.*, 2000) has demonstrated that the ancient city of Sagalassos has been struck by a number of earthquakes during its occupation history. Archaeoseismological evidence (type of damage, extensive and widespread nature of damage) (Sintubin *et al.*, 2003) suggests an intensity of at least VIII (MSK) for the last earthquake(s), causing major damage in the city. An epicentre in the direct proximity, i.e. within a radius of less than 20 km, of the site should be considered (cf. Stiros, 1996). Epicentres of recent and historical earthquakes in the wider area are all located further away from the site (Figure 1). All known active faults in the wider region (Similox-Tohon *et al.*, this volume a) are thus located too far to be considered responsible for the most destructive earthquakes.

In the Aegean region, surface rupturing occurs on normal faults for earthquakes of Ms 5.5 or above (Pavlides and Caputo, 2004). It is fair to assume that the fault(s), responsible for the most destructive earthquakes at the ancient city of Sagalassos, are morphogenic, i.e. have a geomorphological expression. Using diagnostic geomorphological features for active normal faults (Similox-Tohon *et al.*, this volume a) a search for active normal faults within a radius of 20 km from the site has been performed, primarily using remote sensing (Similox-Tohon *et al.*, this volume b). In a number of areas, where active normal faults were positively identified, the remote sensing results have been complemented with surface data and date resulting from near-surface geophysics (Similox-Tohon *et al.*, this volume b).

Similox-Tohon *et al.* (2006) discusses the results of an integrated study on the immediate environment of the archaeological site of Sagalassos, identifying the Sagalassos fault, an active normal fault that may have been the causative fault of the earthquake(s) affecting the city during the late Roman and early Byzantine periods (6th to 7th century AD). In this paper, we discuss the results of an integrated study of the Çanaklı basin, situated some 10 km south of the ancient city of Sagalassos, where a number of lineaments (Similox-Tohon *et al.*, this volume b) may also be potential candidates for the fault(s) causing the destructive earthquakes at Sagalassos (Figures 1 and 2).

2. GEOLOGICAL SETTING

With respect to active geodynamics and seismotectonics the target area is situated at the outskirts of the northeastern extremity of the Fethiye-Burdur fault zone (FBFZ) (Figure 1), a major tectonic feature in SW Turkey (Barka *et al.*, 1995; Bozkurt, 2001; ten Veen, 2004; ten Veen and Kleinspehn, 2002; 2003). Based on recent surveys in the area (Similox-Tohon *et al.*, this volume b; Similox-Tohon *et al.*, 2006; 2007) a new overall, active geodynamic model is proposed in which the study area is situated in a diffuse transfer zone between the Fethiye-Burdur fault zone and the newly defined Isparta-Eğirdir fault zone (IEFZ) (Sintubin *et al.*, in prep).

On the geological map of Senel (1997a; 1997b) (Figures 3 and 4) it is clear that a wide range of lithologies is present in and around the Çanaklı basin (see also Degryse *et al.*, this volume). The subsurface of the area primarily consists of rocks belonging to the Bey Dağları autochthonous units, which are mainly composed of Jurassic to Cenomanian neritic limestone of the Bey Dağları formation, covered by Tertiary flysch deposits (Burdigalian to Lower Langhian). In the northeastern extremity of the area Scynthian to Lower Anisian sandstones crop out, belonging to the Antalya nappes (Figure 4). These nappes are emplaced on top of the Bey Dağları autochthonous domain in Danian times, reflected in the Danian olistostrome unit (Senel, 1997a). Both in the northwest of the area and around the village of Çanaklı rocks belonging to the Lycian nappes are exposed (Figure 4). The Lycian nappes comprise bedrock of Middle Triassic-Liassic limestone, an Upper Senonian ophiolitic mélange and olistostrome unit, covered by Tertiary flysch (Upper Lutetian to Lower Burdigalian) (Senel, 1997a).
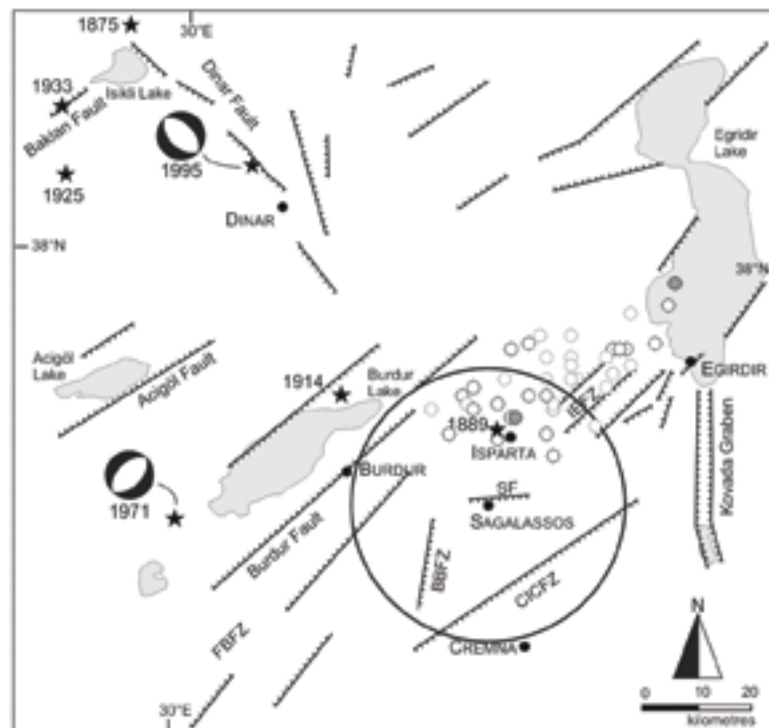
Figure 1: Simplified active fault map of the Lake District centred on Burdur and Isparta at the northeastern extremity of the Fethiye-Burdur fault zone (FBFZ) (after Bozkurt, 2001; Eyidoğan and Barka, 1996; Senel, 1997b), with indication of the epicentres of recent large earthquakes (stars), available focal mechanisms (after Eyidoğan and Barka, 1996; Taymaz and Price, 1992), the microseismic activity in the Isparta-Eğirdir region (white circles are Md 3.0-3.9 events; gray circles are Md 4.0-4.9 events) (KOERI, 2002), and the newly identified fault zones (Similox-Tohon *et al.*, this volume b; Similox-Tohon *et al.*, 2006): the Isparta-Eğirdir fault zone (IEFZ), the Bağsaray-Başköy fault zone (BBFZ), the Çanaklı-Isparta Çayı fault zone (CICFZ), and the Sagalassos fault (SF). Also marked is the target area within a radius of 20 km around the archaeological site of Sagalassos.

The central flat area of the valley is filled by Quaternary alluvial, colluvial and lake deposits (Six, 2004). They are composed of mainly clays and pebbles, gravel and tufa, which originated from weathering and erosion of the surrounding lithologies, i.e. flysch, limestone, ophiolitic mélange, shales, olistostromes and marl with cherts. Soils have vertic properties (Six, 2004).

3. METHODOLOGY

Remote sensing has been performed on a Landsat 7 Enhanced Thematic Mapper + tape and an Ikonos tape. Processing was done using ENVI.

The Landsat 7 tape dates from 9 December 1999 and has a resolution of 30 m for the visible, near-IR and IR bands (1, 2, 3, 4, 5 and 7) and a resolution of 15 m for the panchromatic band (8) (Figure 2). The data were contrast-stretched and filtered. Various combinations of bands were used to try to pick out different features. A combination of bands 4, 5 and 7 for red, green and blue respectively was most widely used as this combination clearly showed the known major active faults (Similox-Tohon *et al.*, this volume a). A fusion of bands 4, 5, 7 and 8 was carried out for an even more detailed image, with the colours of bands 4, 5 and 7 (30 m resolution) and the detail of band 8 (15 m resolution).

The Ikonos tape has a resolution of 4 m for the visible and near-IR bands and of 1 m for the panchromatic band. It covers an area of 8 by 7 km west of the village of Çanaklı (Figure 2). The data were contrast-stretched and filtered. Various combinations of bands were again used to pick out different features. A combination of bands red, green and blue has been used.
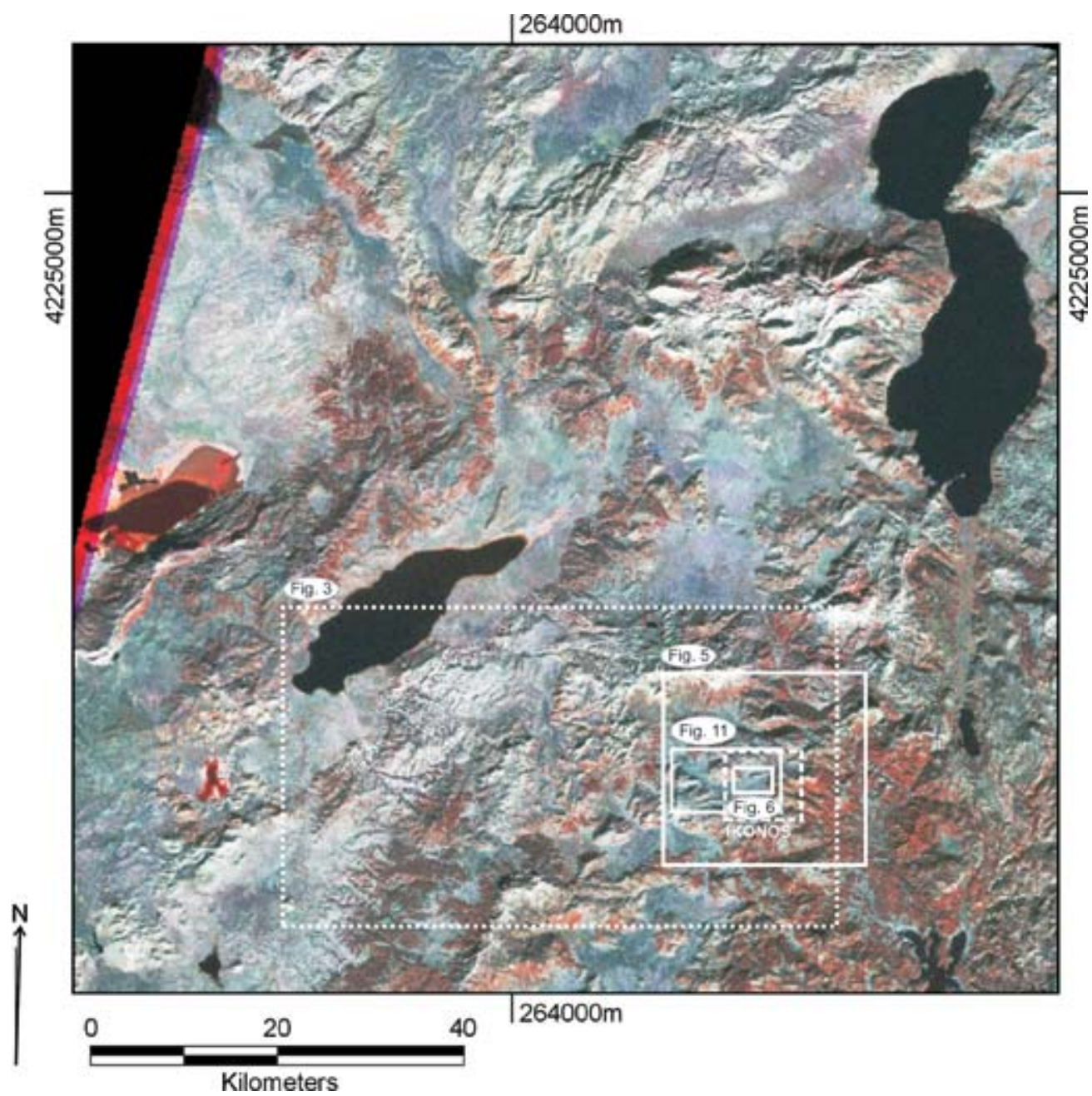
132

Figure 2: Landsat 7 Enhanced Thematic Mapper + image of the Lake District with a combination of bands 4, 5 and 7 for red, green and blue respectively. Projection is UTM Zone 36, Northern Hemisphere (WGS 84). Location of the Ikonos image. Landsat 7 image used in figures 5 and 11. Ikonos image used in figures 6, 11 and 21.

133

Figure 3: Geological map of the territory of Sagalassos (after Senel, 1997b). Active faults, identified based on remote sensing analysis (Similox-Tohon et al., this volume a; Similox-Tohon et al., this volume b) are indicated in red. See figure 2 for location.
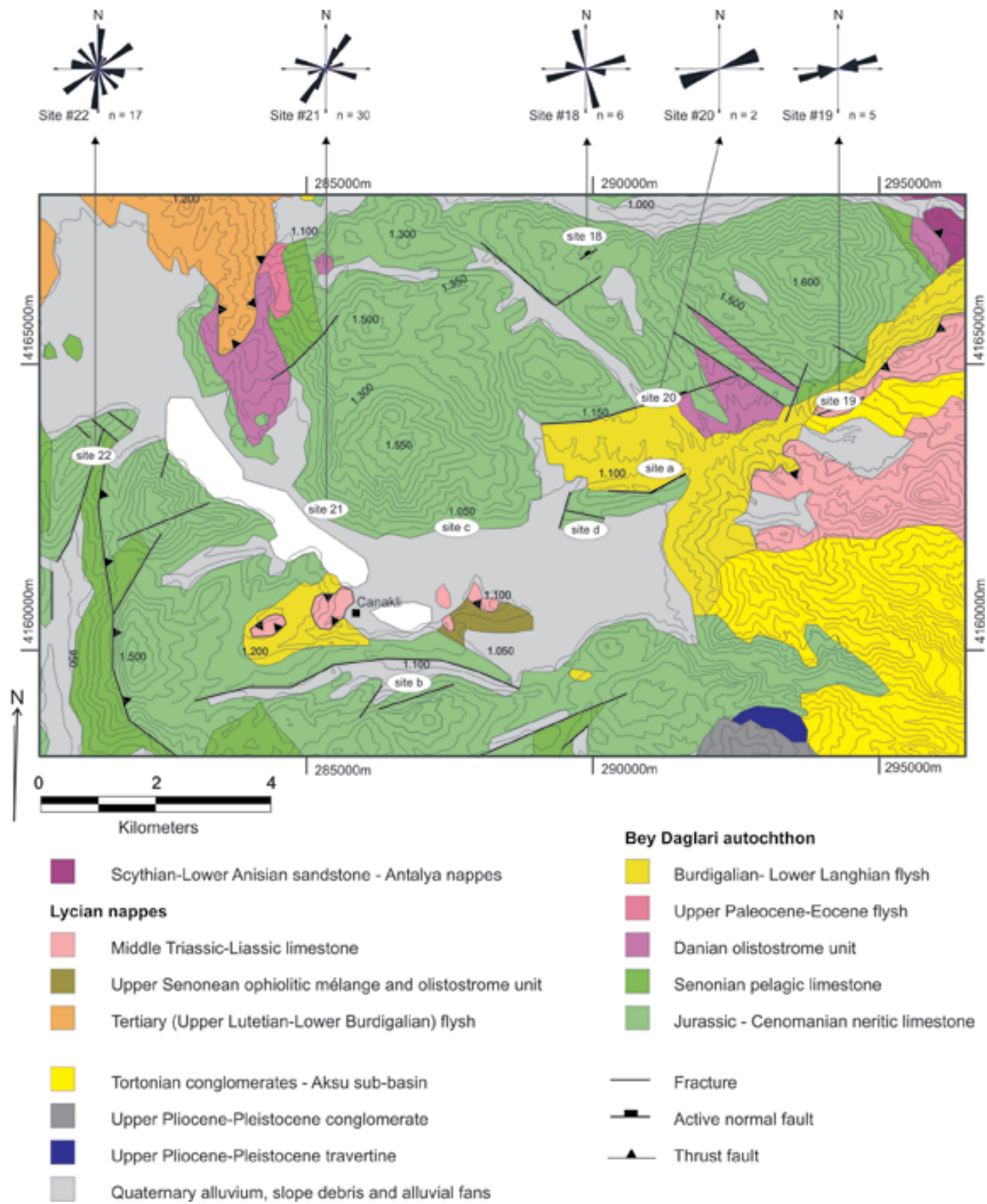
134

Figure 4: Geological map of the Çanaklı basin and surroundings (Senel, 1997a) with indication of fault and fracture data measured at different sites. See figure 3 for location.

135

2D-resistivity imaging has been chosen as the preferred method, not only because this method is reasonably fast, cost-effective and easy to apply in rough terrains, but also because it proved successful in palaeoseismological research (e.g. Camelbeeck and Meghraoui, 1998; Caputo *et al.*, 2004; Caputo *et al.*, 2003; Vanneste *et al.*, 2001) and in archaeoseismological research (e.g. Similox-Tohon *et al.*, 2004).

The resistivity measurements were carried out with the LUND Imaging System of ABEM, which consists of 4 cables of 16 electrodes, branched to a resistivity meter (Terrameter SAS-1000) through an electrode selector (ES-464). Using a roll-along technique, the length of the profile can easily be extended by a multiple of 32 electrodes. All profiles were measured with the standard 64 electrodes. Only profile CA03P01 was extended by roll-along to a total of 96 electrodes. The electrode layout used is a Wenner-Schlumberger layout. This layout is moderately sensitive to both horizontal and vertical structures. It has a rather good penetration and signal/noise ratio but a rather narrow horizontal data coverage (Loke and Barker, 1996). The electrode spacing along the survey line, i.e. the minimum interelectrode spacing, has been chosen to ensure the required resolution and penetration depth, and was in function of the position of the suspected fault along the profile and the space available. The majority of the profiles were measured with the maximum electrode spacing (5 m) that is possible with the LUND Imaging system, enabling large distances to be surveyed and a large penetration depth (50 m). Profile CA03P1 has a spacing of 4 m and profile CA03P5 of 3 m, with penetration depths of 40 m, respectively 30 m. For each data point, the resistivity meter performed a stack of minimum two and maximum four measurements. The standard deviation for each stack is a good indicator of the quality of the data. The quality of most profiles is relatively good to excellent with standard deviations generally below 2.5%. Before proceeding with the inversion, the data set was reduced, i.e. all negative resistivity values were rejected, as well as all data points with a standard deviation above a certain threshold. The filtered data were subsequently re-evaluated visually, and any remaining isolated extreme value was removed. The measured resistivity values do not represent the true subsurface resistivity, but an 'apparent' resistivity, corresponding to the resistivity of a homogeneous subsurface that would produce the same resistance value for the given electrode arrangement (Loke and Barker, 1996). Pseudo-sections plotting the apparent resistivity as a point at the mid-point of the array with respect to depth do not give an accurate image of the true subsurface resistivity, because these plots do not take into account that the signal of each value measured originates form a volume of the

subsurface that depends on the type of array used. The true subsurface resistivity is eventually determined by an inversion. We inverted our data with the commercial Res-2Dlnv software from GEOELECTRICAL. This program iteratively calculates a resistivity model section, trying to minimize the difference between the observed and calculated 'apparent' resistivity. A conventional smoothness-constrained least-squares method has been used for sections CA03P2, CA03P3, and CA03P5. This approach gives optimal results where the subsurface geology shows a smooth variation. It tends, however, to smooth sharp boundaries and to under- or overshoot true resistivity (Loke *et al.*, 2001). The robust or blocky inversion method, on the other hand, has been applied to sections CA03P4, CA03P5 and CA03P6. This approach tends to produce internally homogeneous bodies with sharp boundaries. All inversions were carried out taking into account the topography along the profile. A more detailed description of the method can be found in Similox-Tohon *et al.* (2004).

4. REMOTE SENSING

Based on the analysis of the Landsat 7 Enhanced Thematic Mapper + image (Figure 5), it can be inferred that the Çanaklı basin is situated on a NE-SW trending lineament extending from the Isparta Çayı valley in the northeast to south of the village of Çanaklı over a distance of at least 23 km (cf. Senel, 1997b). This lineament is interpreted to be composed of a series of normal faults, defining the Çanaklı-Isparta Çayı fault zone (CICFZ) (Similox-Tohon *et al.*, this volume b). Contrary to the Isparta Çayı area (Similox-Tohon *et al.*, this volume b) the geomorphological features in and around the Çanaklı basin are not at all obvious.

Northeast of the village of Çanaklı two ca. E-W trending normal faults with opposite dip (F1 and F2; Figure 5) are inferred, exposing in their common hanging wall Burdigalian-Lower Langhian flysch deposits (Bey Dağları formation) from the Bey Dağları autochthonous domain (Senel, 1997b). The sandstone is heavily dissected by a drainage system flowing to the south (Figure 5). Such dissection is considered characteristic for the footwall of an active normal fault since relative uplift is needed to start the dissection process (Similox-Tohon *et al.*, this volume a). Therefore, another active normal fault should be present to the south, in which footwall the sandstone is located. A possible candidate would be the ca. E-W trending northern border of the Çanaklı basin (C1; Figure 5) or a NE-SW trending lineament (C2; Figure 5) crossing the Çanaklı basin. The latter lineament is aligned with the NE-SW trending, SE-dipping fault segments towards the Isparta Çayı valley
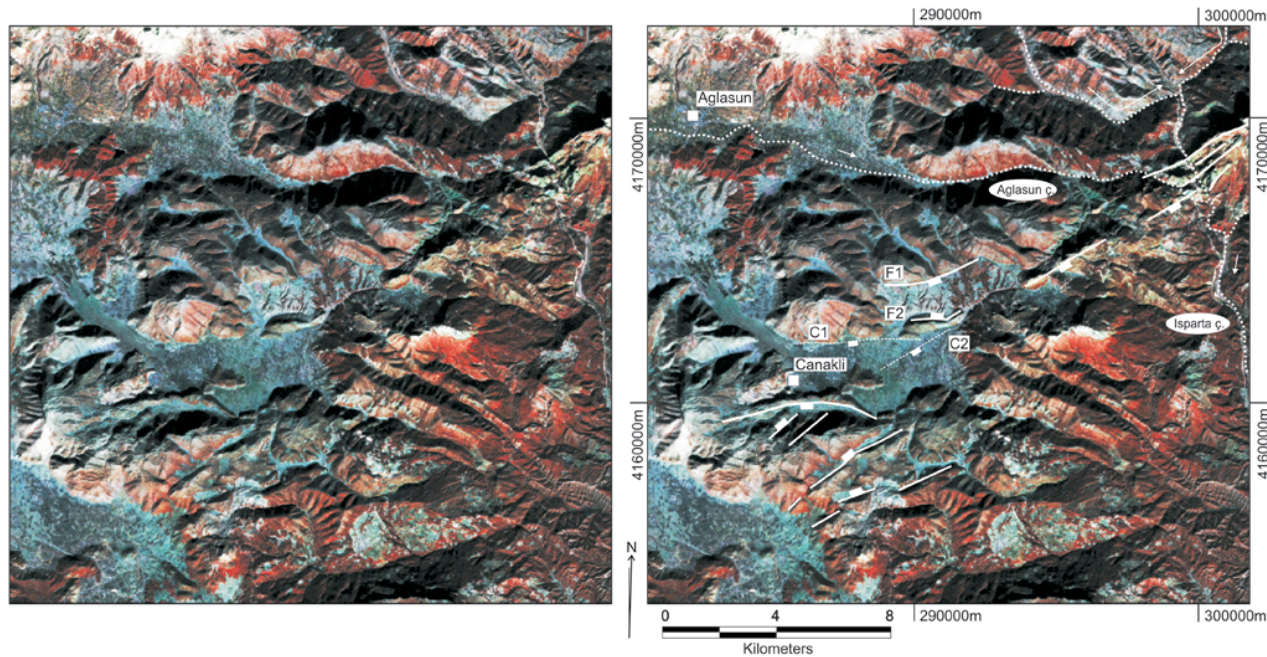
136

Figure 5: Landsat 7 enhanced Thematic Mapper + image with a fusion of bands 4, 5, 7 and 8 of the area centred on the Çanaklı basin in the southwest and the Isparta Çayı in the northeast, showing the traces of the major faults and drainage systems. Projection is UTM Zone 36, Northern Hemisphere (WGS 84). See figure 2 for location.

(Figure 5) (Similox-Tohon *et al.*, this volume b). Both lineaments (C1 and C2) are also apparent on the Ikonos image (Figure 6). The NE-SW trending lineament (C2) is expressed by a slight difference in soil colour, possibly reflecting the presence of different facies on both sides of the lineament. Furthermore, two large alluvial fans entering the Çanaklı basin at its northeastern end can be outlined on this satellite image (Figure 6).

5. SURFACE GEOLOGY

In the wider area in and around the Çanaklı basin a number of sites are investigated looking for evidence of active faulting. The limestones of the Bey Dağları autochthonous domain north and west of the valley (sites 18, 21 and 22; Figure 4) display an intense fracturing (N70E, N30E and N70W trending fracture sets) (Figure 7a). These fractures are often filled with a flowstone-type of calcite precipitate (Figure 7b and c). The limestone escarpment (240/75)[1] at site 18 (Figure 4) juxtaposes limestone and cemented scree (bedding

290/70) (Figure 8). Flowstone-type of calcite precipitated along this contact. In one of the isolated depressions (a few 100 m SE of site 18; Figure 4), conjugate fracture sets were also observed in Quaternary alluvial deposits (Figure 9). Brecciated calcite veins and limestone are abundantly present at the contact. NE of the Çanaklı basin (site 19; Figure 4) a clear limestone escarpment (070/60) (Figure 10a) has been identified. This escarpment aligns with the Isparta Çayı fault scarp to the northeast (Figure 5). No evidence (e.g. fault breccia) has been found for (active) faulting along the escarpment. To the west (site 20; Figure 4), another, less pronounced in height but longer, linear limestone escarpment (N70E) forms the contact between limestone (with thick palisade calcite precipitation) in the north and reddish shales in the south (Figure 10b). Also in this case, no evidence (e.g. fault breccia) has been found for (active) faulting along the escarpment. The isolated limestone massif at the northeastern border of the Çanaklı basin (site a; Figure 4) is limited to the north by an escarpment (240/80) (Figure 10c). This escarpment forms the contact between limestone in the south and a chaotic mélange in the north. Again, no evidence was found for (active) faulting. A limestone mountain range is present south of the Çanaklı basin (site b; Figure 4). In front of the mountain range, a less than 100 year old cedar forest has been planted on slope debris (screes) originating from

---

[1]   Representation of orientation data of planar features uses the 'strike-dip' and 'azimuth' conventions; pitch is counted within the plane starting from strike direction.
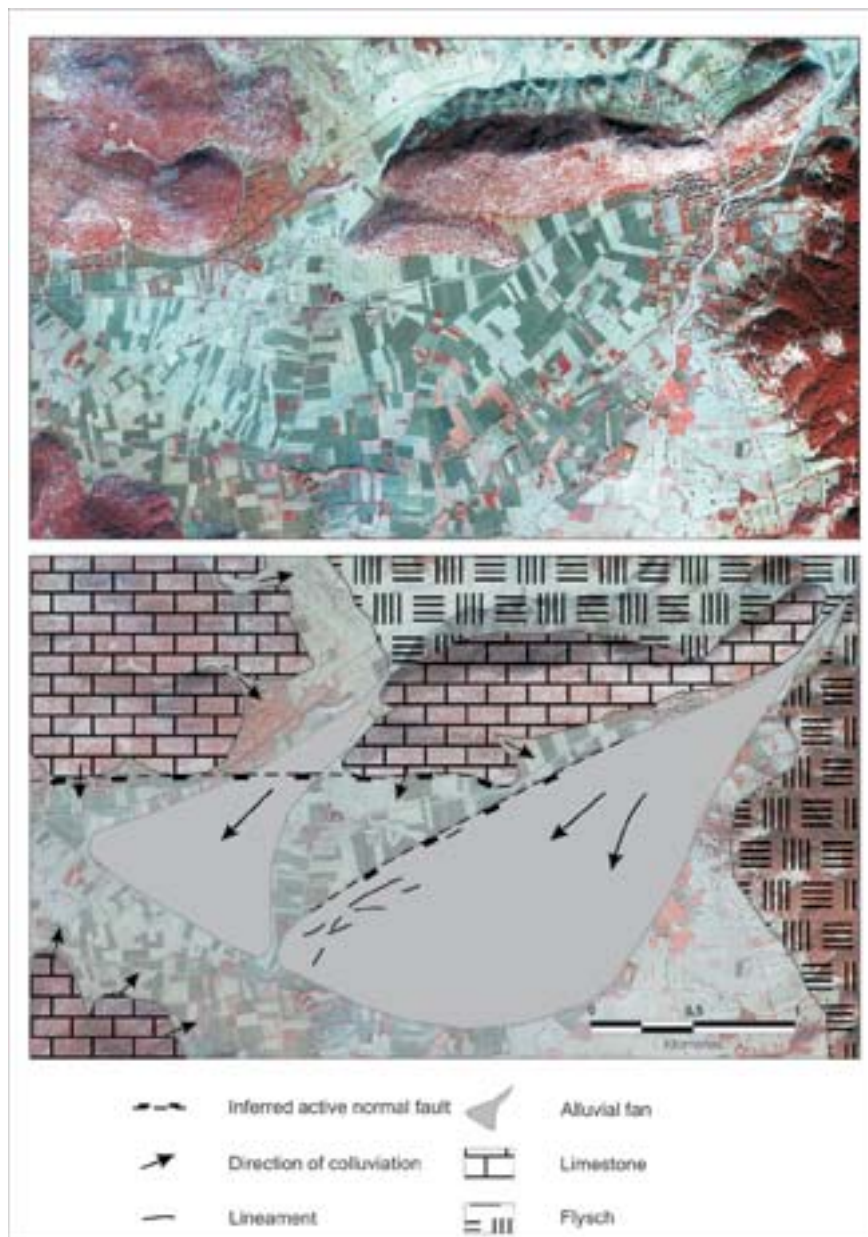
137

Figure 6: Enlarged Ikonos image with a combination of bands red, green and blue of the northern part of the **Çanaklı basin**, showing the lineaments, interpreted as normal fault traces, and alluvial fans. Geological background is taken from figure 4 (Senel, 1997a). See figure 2 for location.
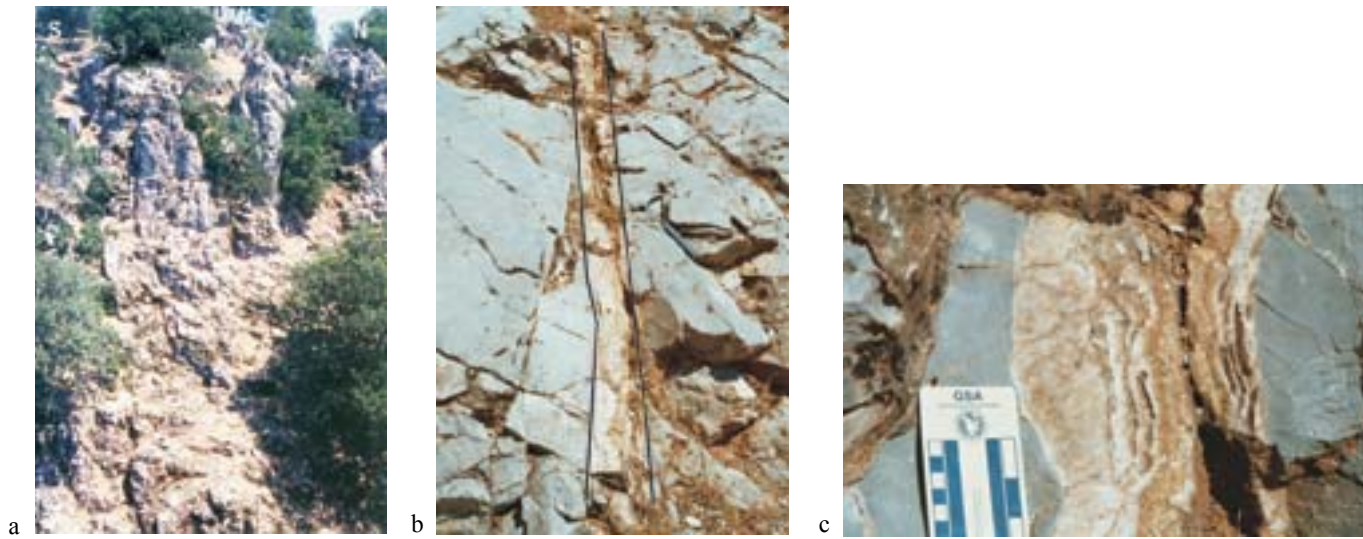
Figure 7: (a) Intense N70E fracture set in Bey Dağları limestone north of the Çanaklı basin (site 18, Figure 4). (b) Large, wide extension vein in limestone with calcite precipitates (hammer = 33 cm long) (site 21, Figure 4). (c) Extension veins filled with crustiform calcites, built up of several, individual parallel calcite layers (site 21, Figure 4).
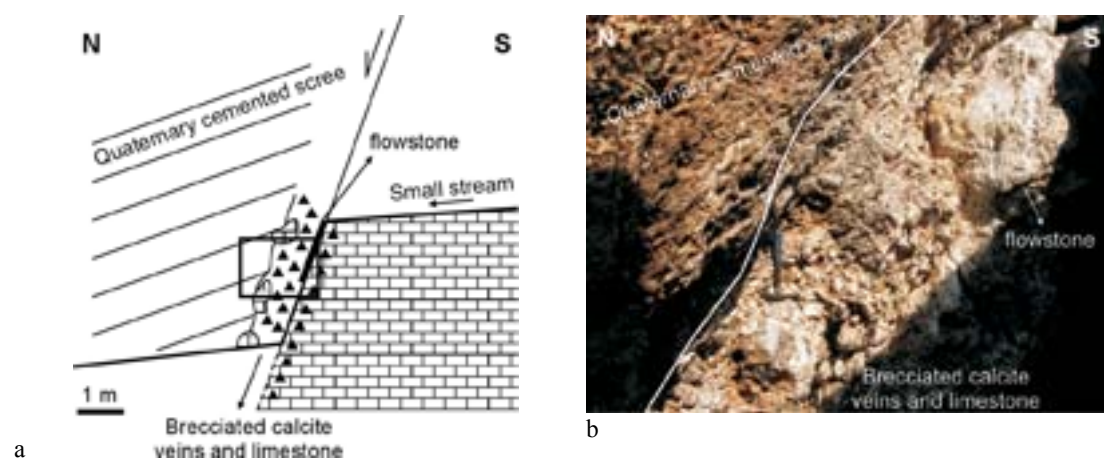

Figure 8: (a) Palaeo-fault scarp (240/75) at the Bey Dağları massif's northern extremity (site 18, Figure 4). (b) Detail of fault zone (see box in a).

Figure 9: Conjugate fracture set, filled with sandy material in the Quaternary alluvial deposits (hammer = 33 cm long) (site situated some 100 m SE of site 18; Figure 4).

139

Figure 10: (a) Limestone escarpment (070/60) (site 19; Figure 4). (b) Limestone escarpment (N70E) (site 20; Figure 4). (c) Limestone escarpment (240/80) (site a; Figure 4). (d) Limestone mountain range south of the Çanaklı basin (site b; Figure 4). (e) Fault breccia along the E-W trending limestone front (site c; Figure 4). (f) Small elevated (ca. 10 m above valley floor) terrace in the footwall part of the E-W trending limestone front (site d; Figure 4).
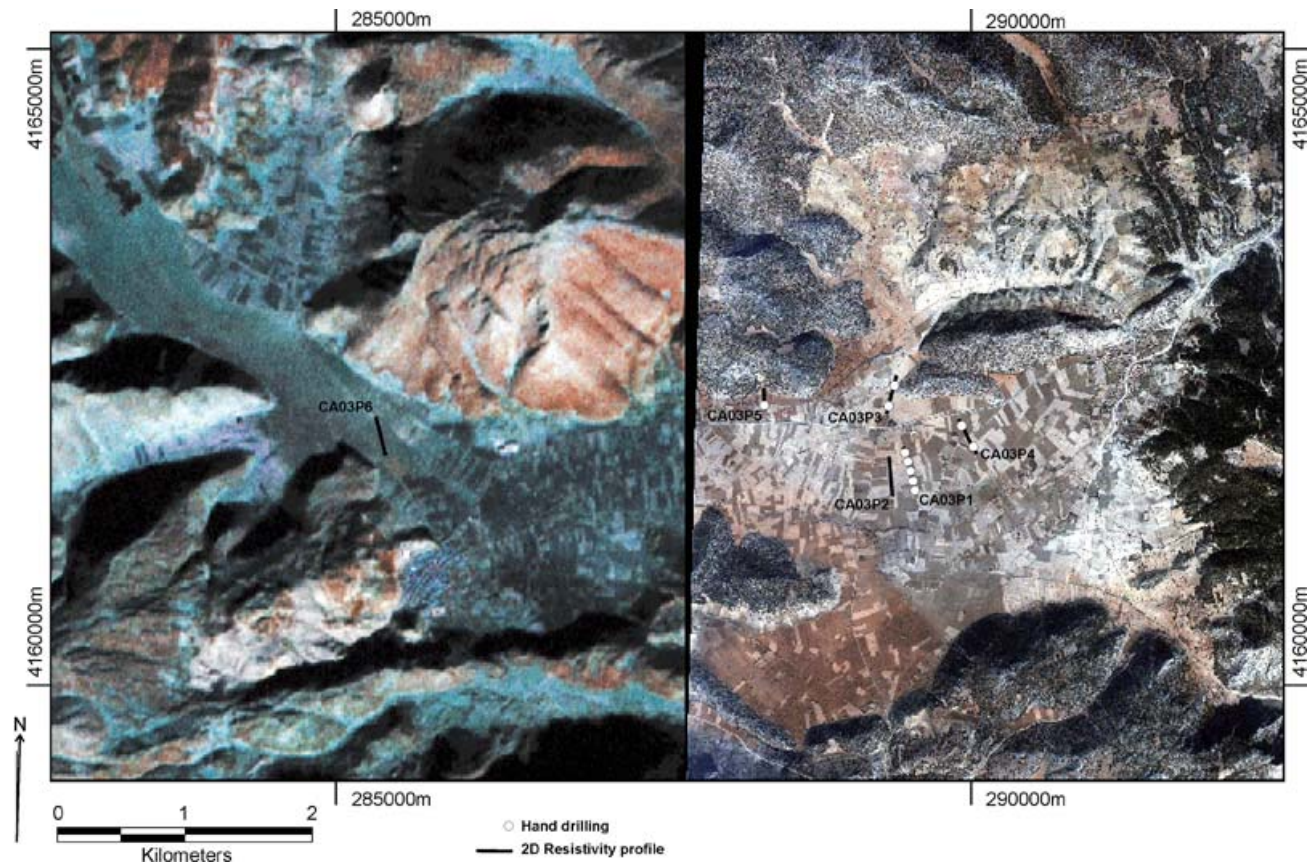
140

Figure 11: Combined satellite image of the Çanaklı basin with location of the six 2D-resistivity profiles and the ten hand drillings along the profiles. Left part of the image is a Landsat 7 Enhanced Thematic Mapper + image with a fusion of bands 4, 5, 7 and 8. Right part of the image is an Ikonos image with a combination of bands red, green and blue. Projection is UTM Zone 36, Northern Hemisphere (WGS 84). See figure 2 for location.

the mountain range (Figure 10d). In front of the forest and screes, reddish clay deposits, until recently used for producing local ceramics, are present in very irregular hills in the depression between the surrounding limestone outcrops. Again, there is no evidence of (active) faulting. A distinct E-W-trending front also occurs north of the Çanaklı basin (site c; Figure 4), also apparent as a clear lineament (C1; Figure 6) on satellite images. Here a fault breccia has been encountered on the E-W-trending limestone front, suggesting the presence of a(n) (active) (normal) fault (Figure 10e) (cf. Stewart and Hancock, 1990). Small elevated (alluvial?) terraces were observed in the footwall part of this lineament (site d; Figure 4). However, these steps could equally be man-made terraces and/or ancient walk levels to by-pass a swamp or periodical lake (Paulissen pers. comm., 2004) (Figure 10f).

6. NEAR-SURFACE GEOPHYSICS: 2D RESISTIVITY IMAGING

The geophysical analysis focuses on two lineaments: (1) the E-W trending lineament (C1) delimiting the Çanaklı basin to the north, apparent on both satellite images (Figure 6) and in the landscape as a clear escarpment bearing indications of active faulting (Figure 10e-f); and (2) the NE-SW trending lineament (C2) crossing the valley (Figure 6), lacking any geomorphological expression. 2D-resistivity imaging is used to image the subsurface, eventually to detect any evidence of historical or recent fault activity.

In total 6 profiles were measured, 1 of 380 m (using a roll-along technique), 1 of 189 m and 4 of 315 m (Figure 11). The relevant acquisition parameters can be found in Table 1. The topography has been taken into account for each profile. An impression of different settings is given

141

Nr.	Locality	Nel	dE(m)	Layout	Length	Orientation	Investigation depth	Data quality
CA03P1	Çanaklı	96	4	WSC	380	S-N	40	bad
CA03P2	Çanaklı	64	5	WSC	315	S-N	50	good
CA03P3	Çanaklı	64	5	WSC	315	S-N	50	excellent
CA03P4	Çanaklı	64	5	WSC	315	S-N	50	good
CA03P5	Çanaklı	64	3	WSC	189	S-N	30	medium-good
CA03P6	Çanaklı	64	5	WSC	315	S-N	50	good

Table 1: Relevant acquisition parameters for the 2D-resistivity profiles. Nel = number of electrodes. dE (m) = electrode spacing in meters. WSC = Wenner-Schlumberger layout.
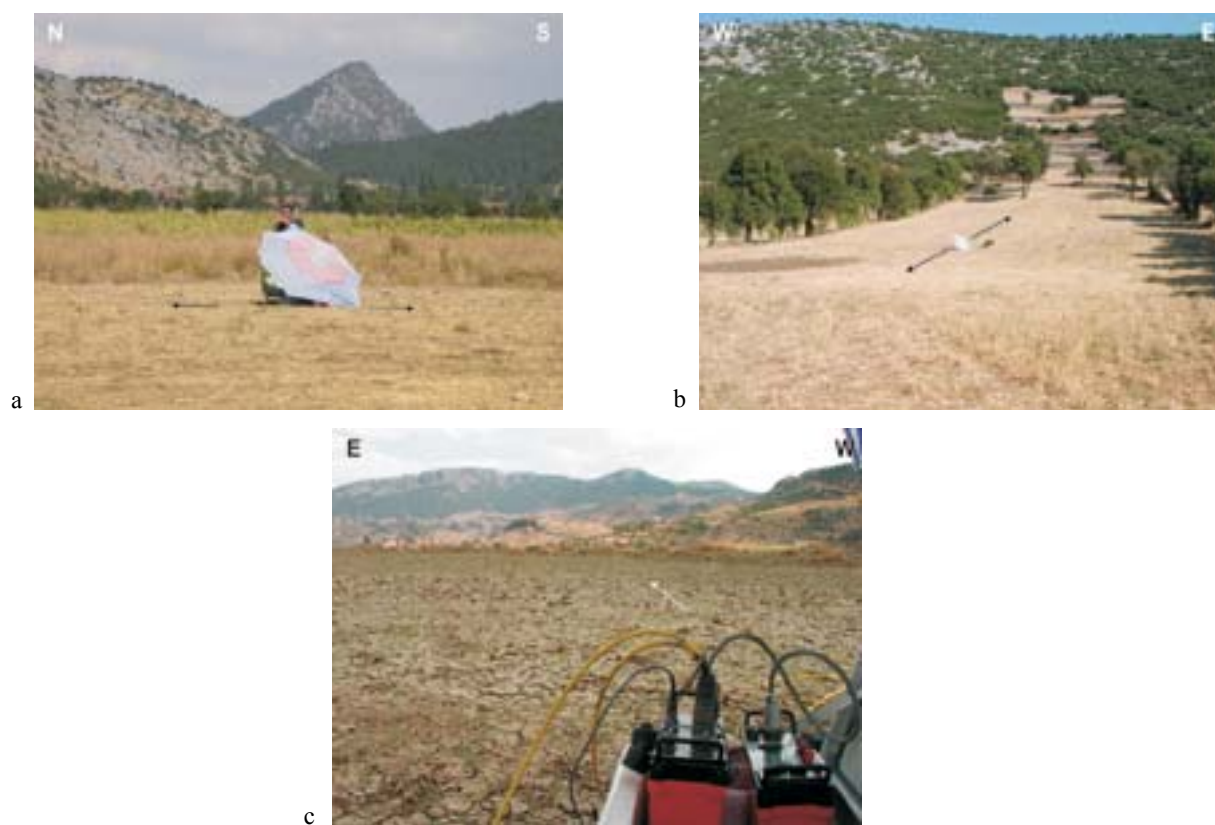

Figure 12: (a) View of profile CA03P4. (b) View of profile CA03P5. (c) View of profile CA03P6. Arrows indicate direction of cable layout. See figure 11 for location of profiles.

in figure 12. In total 10 hand drillings (up to 4 m depth) were performed to constrain the lithological composition of the upper part of several profiles (Figures 11 and 13). Profiles CA03P3, CA03P5 and CA03P6 concern lineament C1. While profiles CA03P3 and CA03P5 are located in front of the limestone escarpment and are oriented nearly perpendicular to the escarpment approximately down-slope, the profile CA03P6 is located on the valley floor, potentially crossing the western continuation of the lineament. Profiles CA03P1, CA03P2 and CA03P4 concern lineament C2 and are oriented nearly perpendicular to this lineament.
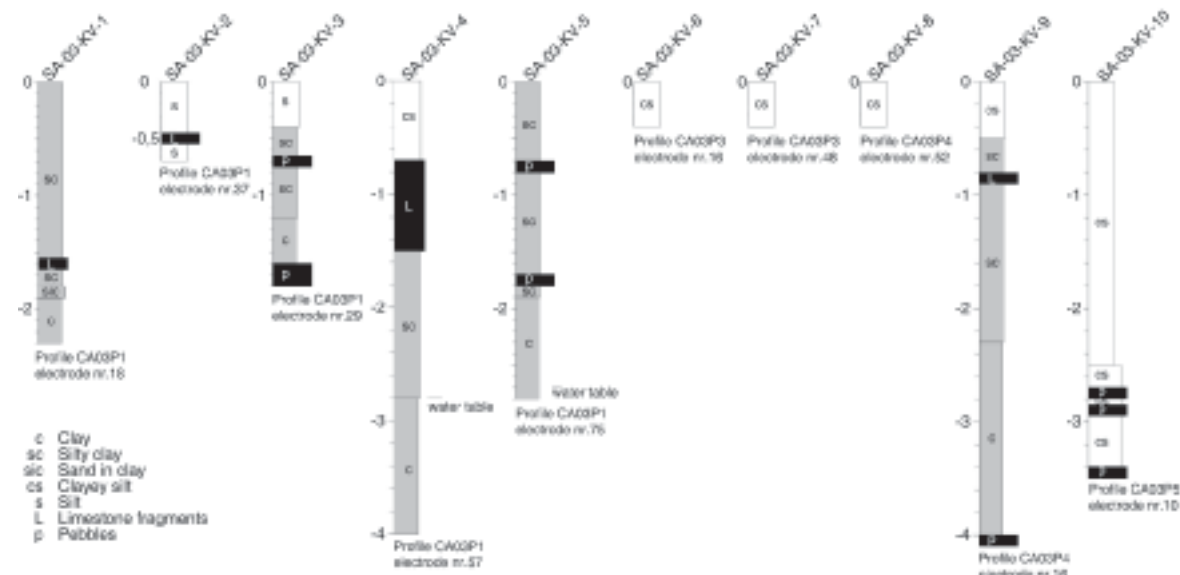
142

Figure 13: Overview of hand drillings in the Çanaklı basin. SA-03-KV-1 to SA-03-KV-5 are five drillings located along profile CA03P1. Drillings SA-03-KV-6 and SA-03-KV-7 are located along profile CA03P3 (Figure 15). Drillings SA-03-KV-8 and SA-03-KV-9 are located along profile CA03P4 (Figure 16). Drillings SA-03-KV-10 is located along profile CA03P5 (Figure 17 and 18). The electrode number is indicated each time. The location of the profiles is indicated on figure 11.

6.1. Profile CA03P1

Extreme high error % (standard deviation between the same measurements) occurred during several measuring slices. This problem is due to an overheating of the ABEM resistivity meter. The data can be considered to be useless. To overcome this problem the next days, the measuring device was put in the shade and Imax was lowered. Five hand drillings were carried out, with a maximum depth of 4 m (Figures 11 and 13). The first metres consist of silt and silty clays (Figure 13), below which pure wet and compact clays are present. According to a local farmer a phreatic zone is reached at 8 m depth around electrode nr. 1.

6.2. Profile CA03P2

The lowest resistivity (1-40 Ωm) is believed to represent (wet) clay (up to 45 m depth) (Figure 14). It corresponds with the Quaternary fill of the Çanaklı basin. These clays may have accumulated in periodical lakes and/or by clay supported alluvial fans originating from the surrounding hills (Paulissen pers. comm., 2004). Higher-resistivity zones (80 Ωm) are incised in the low-resistivity material (Figure 14). They are interpreted as river gullies. The gully at metre mark 70 (Figure 14) corresponds with one of the secondary lineaments on the Ikonos image (Figure 6). We therefore assume that those lineaments do not correspond with

secondary faults but represent abandoned river beds. The most northern higher-resistivity zone can correspond to the alluvium north of the main lineament (C2), as defined on the Ikonos image (Figure 6). This main lineament crosses the profile around electrode nr. 40 at metre mark 200 (Figure 14). No evidence of a fault is observed at this point. The spectral difference on the Ikonos image between the alluvium north and south of the main lineament (Figure 6), can thus be attributed to a different origin of the deposits and not to fault activity (Paulissen pers. comm., 2004). The alluvium north of the main lineament is a direct result of weathering and erosion of the surrounding limestone. The alluvium south of the main lineament can be interpreted as major debris cones originating from flysch hills in the NE. Its direction of transport corresponds to the small actual topographic inclination. However, no subsurface morphological features of such a cone were observed on the resistivity profiles (Figure 14). The abandoned riverbeds are located within and parallel to the debris cone. They may attest of a more active (ephemeral) river system in earlier times, as already suggested by Six (2004) for the western part of the valley. No drillings were carried out along this profile.

6.3. Profile CA03P3

This profile lies nearly perpendicular to the limestone escarpment bordering the valley to the north and is centred with
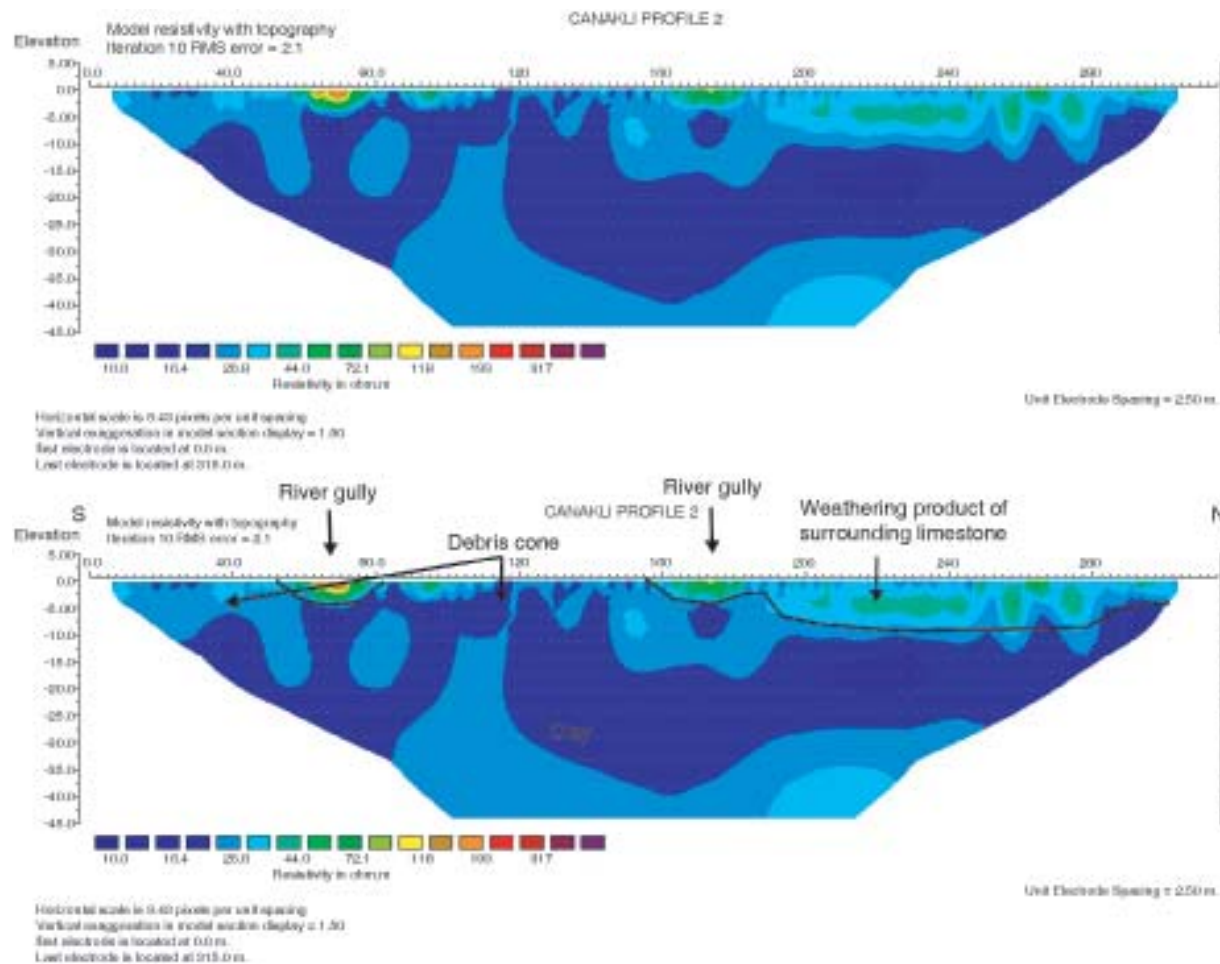
143

Figure 14: Conventional inversion for profile CA03P2 with a uniform colour scale for all Çanaklı profiles, and with interpretation. See figure 11 for location.

respect to this lineament. The limestone front, at metre mark 130 (Figure 15), north of the depression is apparent as a very sharp and straight, steeply S-dipping contact between high-resistivity material (limestone) to the N and low-resistivity material (clay/silt) to the S. The northern border of the depression seems clearly fault controlled. Some evidence is present on the resistivity profile that may infer an active normal fault: (1) in the hanging wall, a wedge-shaped body (Figure 15) is observed, which is probably related to surface faulting, i.e. colluvial wedge(s); and (2) resistivity layers in the hanging wall block seem to be vertically displaced by a set of subsidiary 'antithetic' normal faults (Figure 15). Quaternary activity on these faults may have occurred. As no topographical scarp is present, faulting must be older than the most recent deposits. These deposits are possible very young as indicated in Six (2004), which dates the upper 4.6 m sediments in a sediment core near profile CA03P6 as Late Holocene (< 1000 BC). The

resistivity values of the deepest layer in the hanging wall (Figure 15) correspond with those of the weathering product of the surrounding limestone observed in the CA03P02 profile (Figure 14), which lies in the southern prolongation of the CA03P03 profile (Figure 11). However, the thickness of this layer extends here up to a depth of 45 m. The resistivity values near the surface cannot well be correlated with the observations on the Ikonos image (Figure 6). The resistivity profile crosses the contact between a debris cone originating from the NE, in the north, and alluvium corresponding to the erosion product from the limestone, in the south. No evidence of such a cone can be seen on the resistivity profiles (Figure 15). Moreover, the surface resistivity values can be divided in three, instead of two zones. The central zone with higher resistivity values can be linked to the proximity of the outcropping limestone to the east and may be interpreted as a colluvium originating from this limestone. Two hand drillings were carried out,
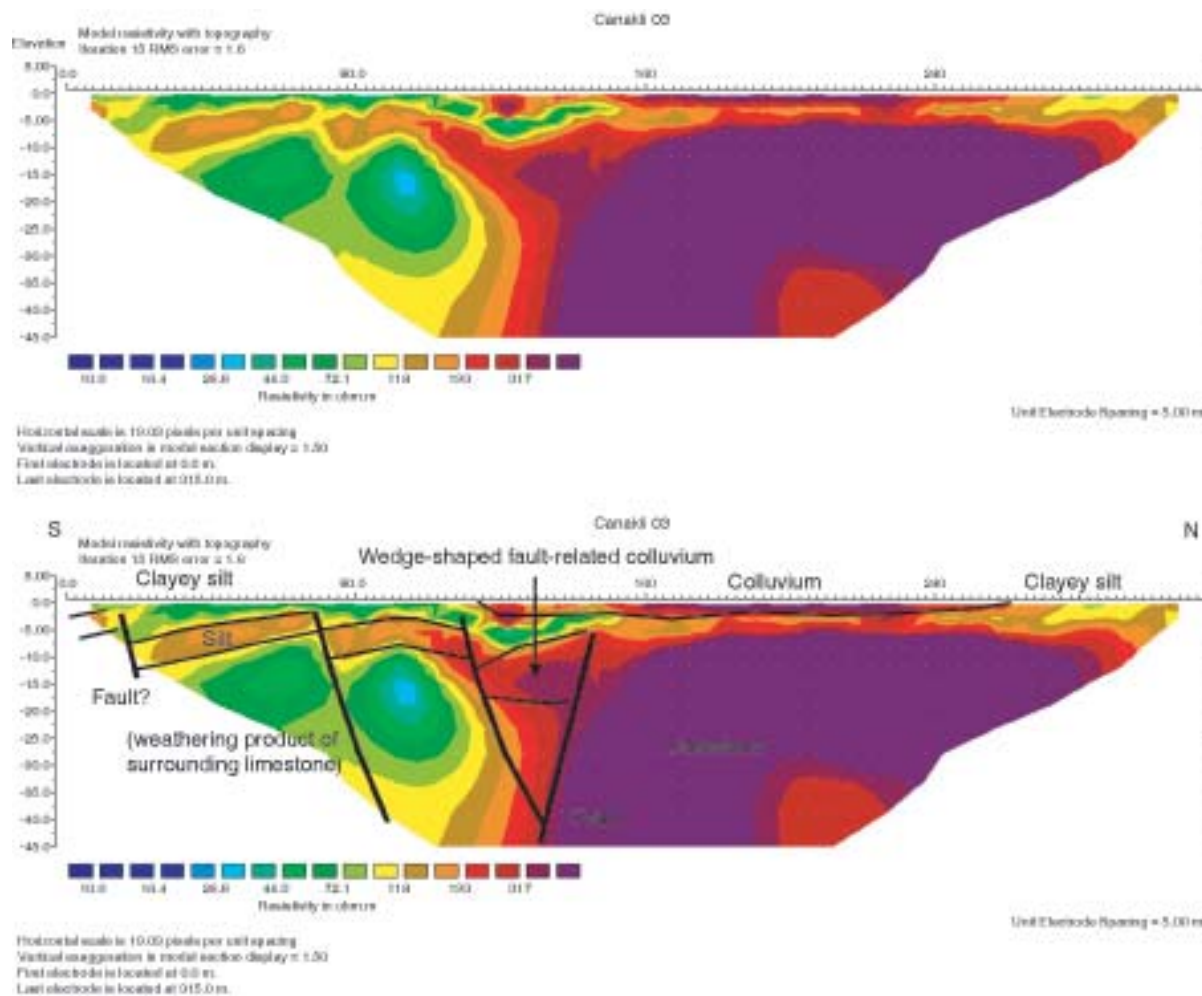
144

Figure 15: Conventional inversion for profile CA03P3 with a uniform colour scale for all Çanaklı profiles, and with interpretation. See figure 11 for location.

with a maximum depth of 40 cm (Figure 13). The upper 40 cm consist of clayey silt with small limestone fragments. No water table was reached.

6.4. Profile CA03P4

This profile lies perpendicular to lineament C2, to the east of profile CA03P2. It is somewhat similar to the profile CA03P2. Very low resistivity values are dominant up to a depth of 45 m (Figure 16). A surface layer with slightly higher resistivity values is present (Figure 16). This layer is more than 5 m thick in the N and gradually dies out to the S. A high-resistivity body is present around electrode nr. 40-41 / metre mark 202 in this surface layer (Figure 16). At this location a secondary lineament was observed on the Ikonos image (Figure 6). This high-resistivity body is interpreted as a river gully. No evidence of faulting is observed at the contact between the alluvium type N of the main lineament and the alluvium type S of the main lineament. Two hand drillings with a maximum depth of 4 m (Figure 13) indicate that the surface layer is composed of clays and silt with limestone fragments, while the lower resistivity values represent rather pure clays. The water table has not been reached.

6.5. Profile CA03P5

This profile is located along the northern border of the Çanaklı basin, to the W of profile CA03P3. It is also similar to it. A very sharp and straight, steeply S-dipping contact between high-resistivity material (limestone) to the north and low-resistivity material (clay/silt) to the south is observed (Figures 17 and 18). This is a clearly fault-controlled contact. This fault, around metre mark 80 (Figures 17 and 18),
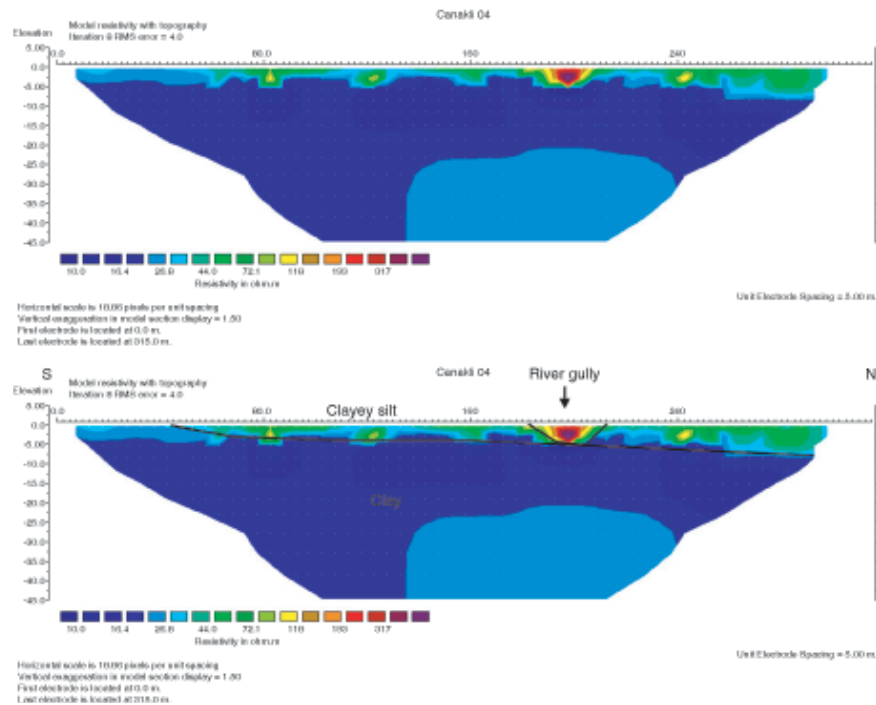
145

Figure 16: Robust inversion for profile CA03P4 with a uniform colour scale for all Çanaklı profiles, and with interpretation. See figure 11 for location.
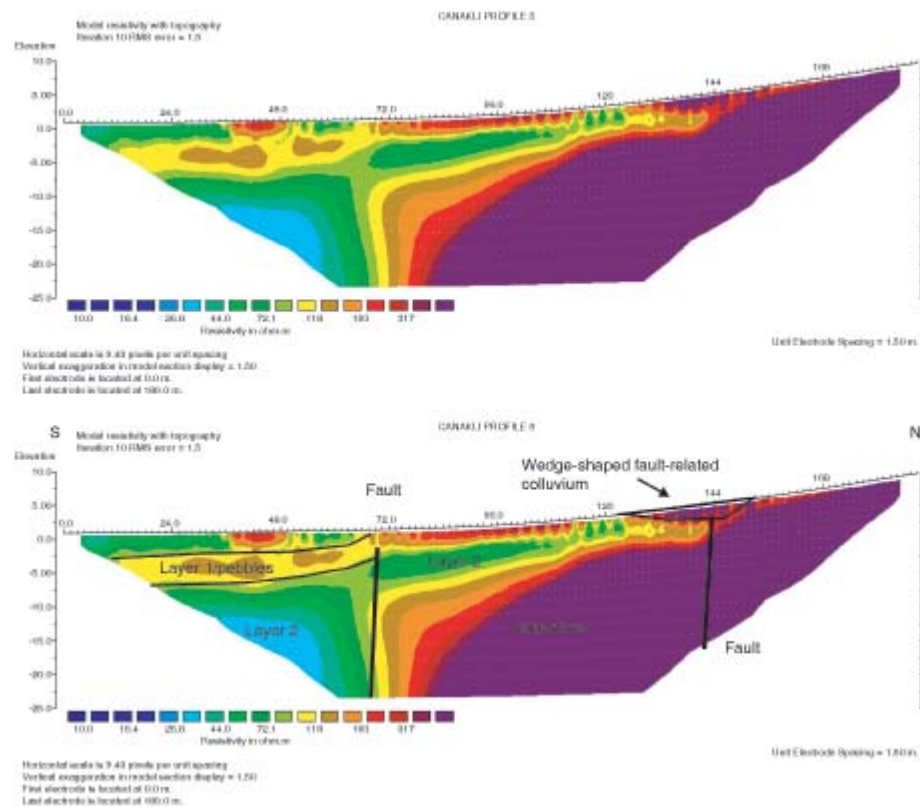

Figure 17: Conventional inversion for profile CA03P5 with a uniform colour scale for all Çanaklı profiles, and with interpretation. See figure 11 for location.
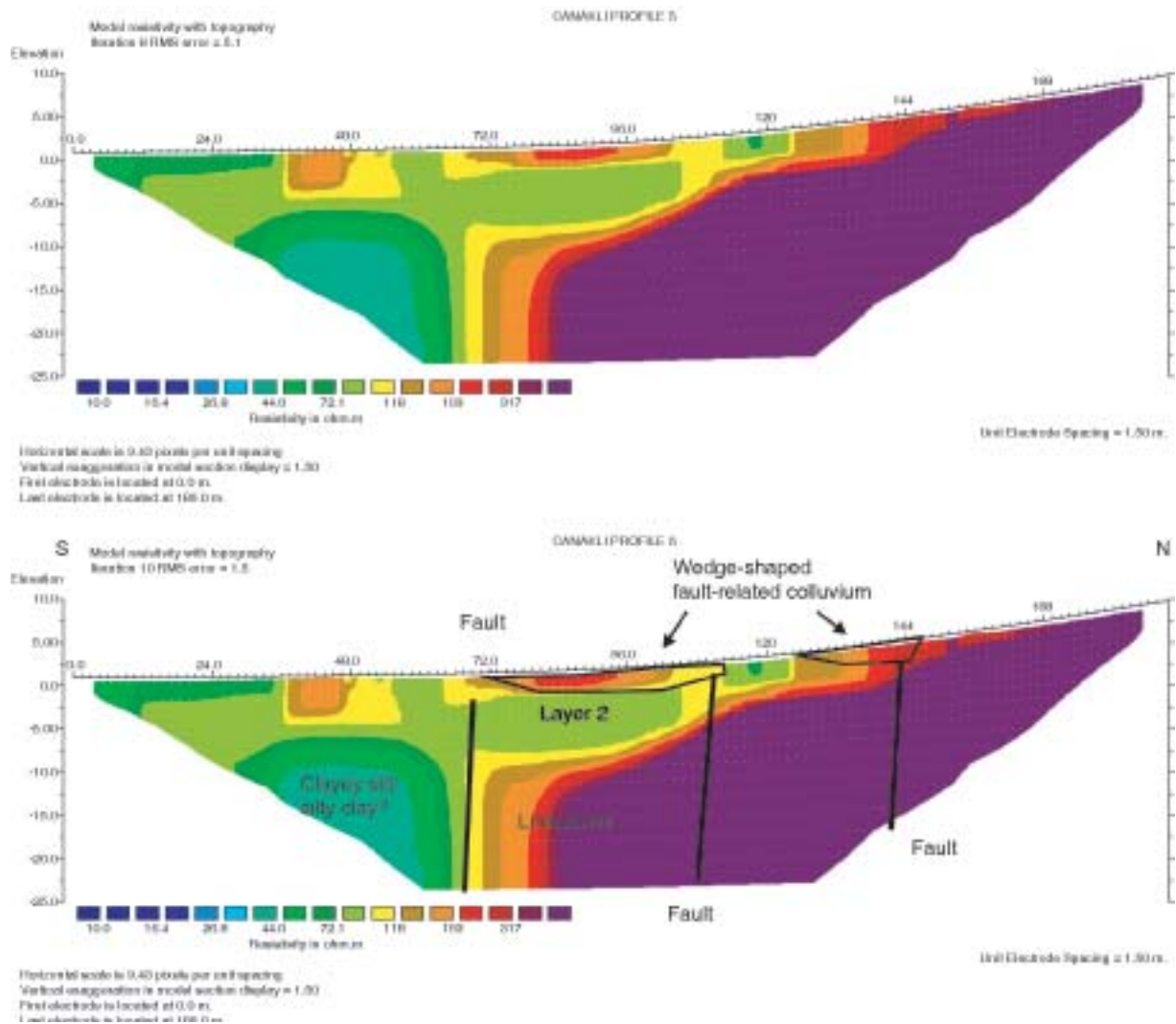
146

Figure 18: Robust inversion for profile CA03P5 with a uniform colour scale for all Çanaklı profiles, and with interpretation. See figure 11 for location.

corresponds with the location of the limestone front at the surface. Two additional 'synthetic ' normal faults can be observed in the footwall, as the top of the limestone bedrock displays vertical offsets (Figures 17 and 18). Some evidence is present that these faults may be interpreted as active normal faults: (1) in the hanging wall of the two most northern faults, wedge-shaped bodies are observed, which are probably related to surface faulting (Figures 17 and 18), i.e. colluvial wedges; (2) a knick-point is present in the topography, between electrode nr. 43 and 47, above the most northern wedge-shaped body and could represent a small degraded fault scarp (Figures 17 and 18); and (3) on the conventional inversion (Figures 17) a resistivity layer in the hanging wall seems to be vertically displaced

at the main fault. The resistivity values of the deepest part of the hanging wall correspond with those of the weathering product of the surrounding limestone observed in the CA03P2 and CA03P3 profile. One hand drilling has been carried out around electrode nr. 10 (Figures 13 and 17). The upper most drilled material consists of brown clayey silt with rounded limestone fragments (up to 7 cm) and small pebbles. Layer 1 on the conventional inversion (Figure 17) corresponds with an increase in pebbles and sand (cf. drilling SA03KV10). These fluviatile pebbles and sands may also testify to a more active (ephemeral) river system in earlier times, as already suggested by Six (2004) for the western part of the valley.
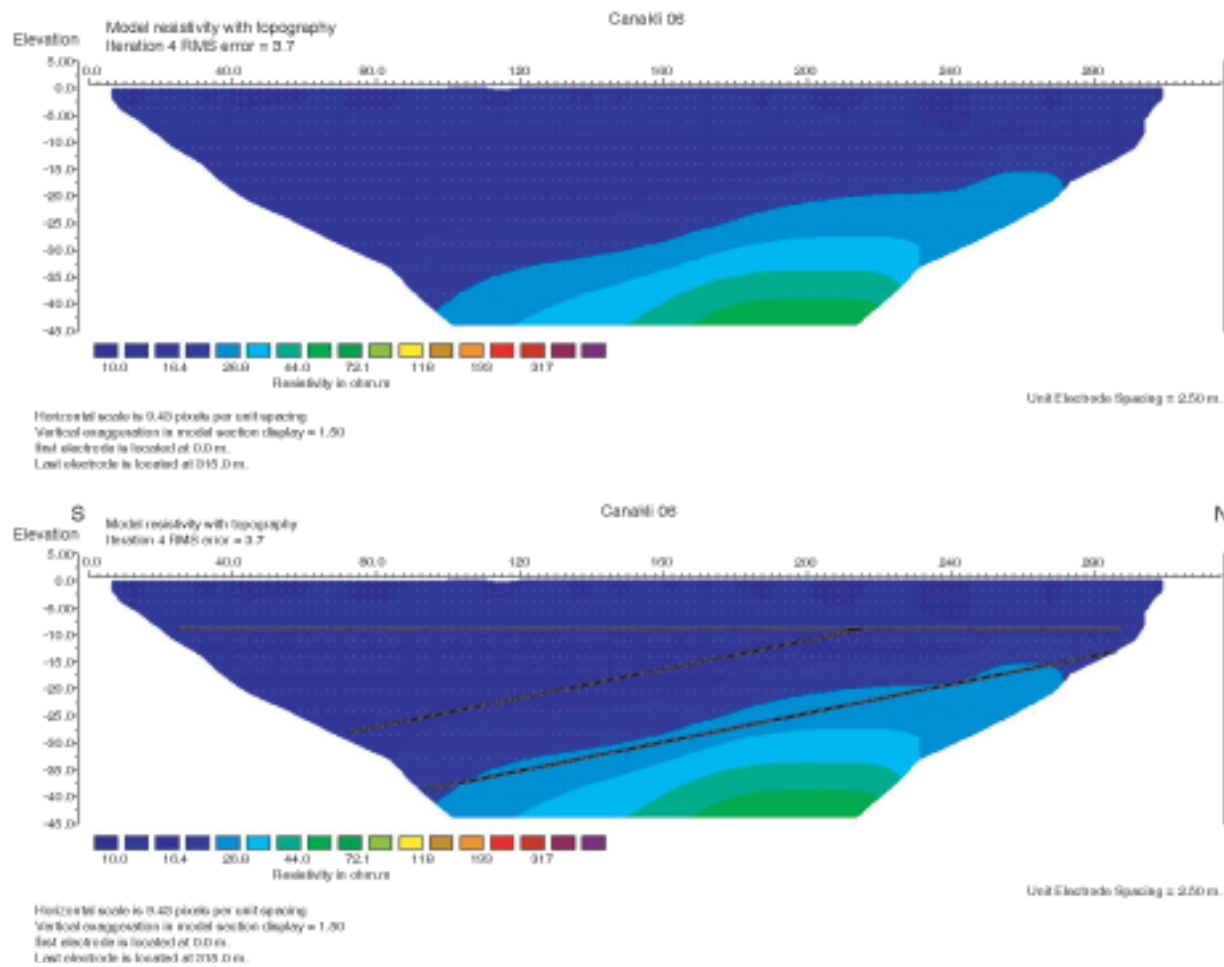
147

Figure 19: Robust inversion for profile CA03P6 with a uniform colour scale for all Çanaklı profiles, and with interpretation. See figure 11 for location.

6.6. Profile CA03P6

The CA03P6 profile was laid out at the western continuation of the normal fault detected on the profiles CA03P3 and CA03P5. This profile lies totally within the Çanaklı basin and allows us to investigate if this fault affects the Quaternary sediments within this basin. On the resistivity profiles we observe that a very thick sequence of clay is present (Figure 19). A surface layer displays a horizontal stratification, while the deeper layers show a tilted stratification towards the south and an increase in resistivity value (Figure 19). The small variation in resistivity does not allow to exclude or to prove the presence of a fault. However, there is no surface evidence for a fault scarp. This excludes fault reactivation since the youngest sediments are not affected. These deposits are very young, as indicated by Six (2004), who dates the upper 4.6 m sediments in a sediment core near profile CA03P6 as Late Holocene

(< 1000 BC). Hence, there is no evidence of recent (< 1000 BC) reactivation. The sedimentary fill of the valley is supposed to be subhorizontal or has a small slope basin inwards (Paulissen pers. comm., 2004). The tilted stratification (11°) of the deeper layers (Figure 19) is, however, too high and may reflect older tectonic activity. This is e.g. the case for the Burdur Formation which dips 10-15° as a result of basin-controlling fault activity (cf. Price and Scott, 1991). The location of any active fault can not be deduced based on these observations alone. The presence of a major antithetic fault to the south of the CA03P6 profile, responsible for the observed (back-)tilt, is highly hypothetical. No additional drillings were carried out along the profile.

6.7. Interpretation of 2D resistivity imaging

Clay deposits characterize the Çanaklı basin. Hand drillings show the presence of a water table at shallow depth.
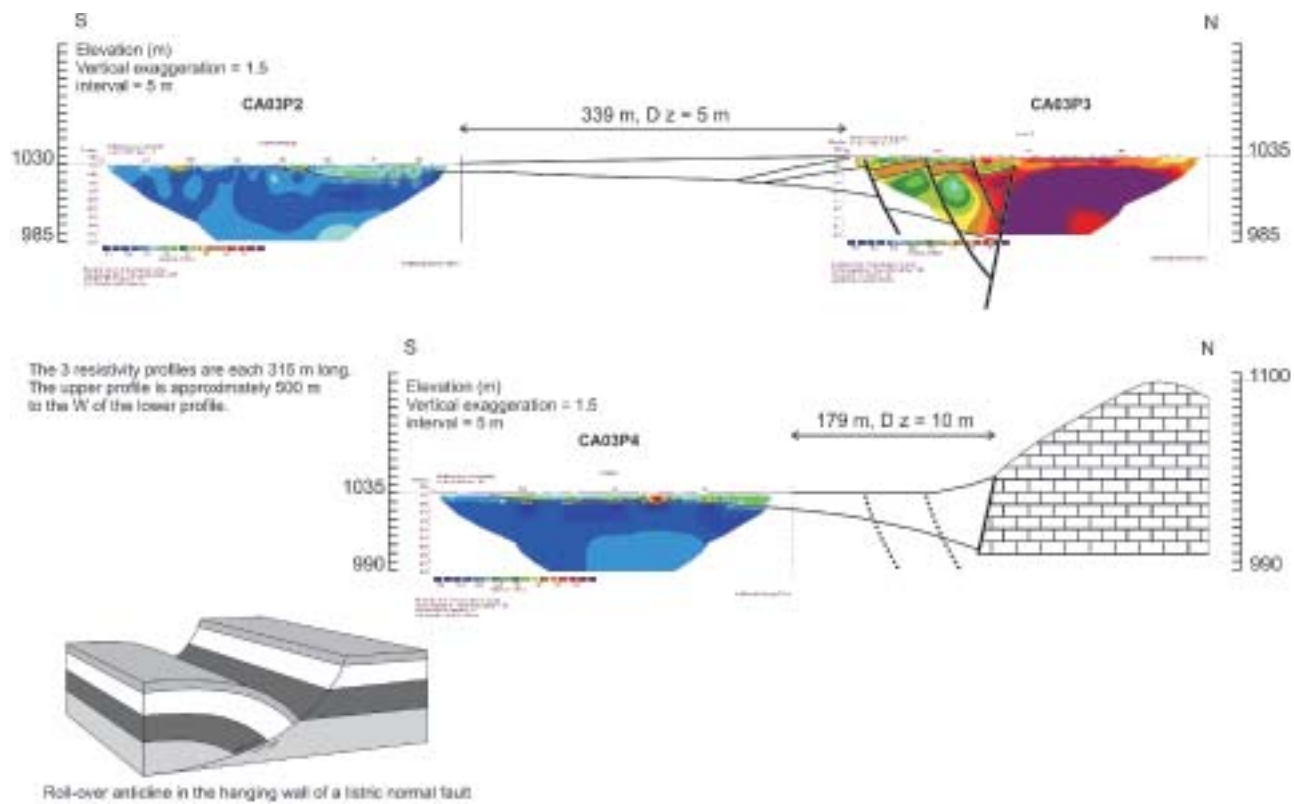
148

Figure 20: Correlation of the N-S profiles (CA03P2, CA03P3 and CA03P4) along the northern edge of the Çanaklı basin, possibly inferring a roll-over anticlinal architecture in the hanging wall of a listric normal fault.

The resistivity profiles demonstrate that the basin is filled with at least 45 m of (wet) clays. This extremely thick sequence of low-resistivity (1-60 Ωm) material did not affect the quality of the measurements (standard deviation mostly below 2.5%). Near the surface, a more silt-rich layer can be observed, which displays slightly higher resistivity values. This surface layer is not more than 10 m thick in the depression, but represents a layer of at least 45 m close to the fault-controlled northern border of the valley. The contrast in thickness may be due to a roll-over anticline in the hanging wall of this normal fault (Figure 20). In areas where flat-lying beds are deformed by normal faults, roll-over folds in the hanging wall block are common. In these folds, the beds in the hanging wall block tilt down into the fault. They form on listric normal faults. As the hanging wall block slips on the fault, it deforms to maintain contact with the footwall block across the fault, thereby producing a bend in the layering. The presence of a rollover anticline, subsidiary 'antithetic' normal faults and wedge-shaped fault-related colluvium in the basin deposits suggest that displacement on the listric normal fault occurred during sedimentation, i.e. a growth fault (Figure 20). However,

there is no evidence on the profiles that this fault affected the youngest (Late Holocene) sedimentary filling of the valley. Still, Six (2004) invokes tectonic activity to explain the much more pronounced recent accumulation in a core near profile CA03P6 in comparison to 2 other cores more northwards. A listric fault geometry for the Burdur fault is also pointed out by Price and Scott (1991) based on the difference in plunge at surface and at the hypocentre of the 1971 Burdur earthquake (fault-plane solution).

The continuation of the Isparta Çayı lineament into the Quaternary Çanaklı basin did not show up at all in the resistivity profiles. No evidence of faulting is present within the Çanaklı basin. The spectral differences of the basin on the Ikonos image are due to a different origin of the deposits. Some of the secondary lineaments observed by the remote sensing correspond with river gullies that display a higher resistivity (Figure 21). The presence of these gullies, the 2 debris cones originating from the flysch hills in the northeast (Figure 21) and the fluviatile pebbles and sand observed in hand drillings, suggest the presence of a more active river system in earlier times.
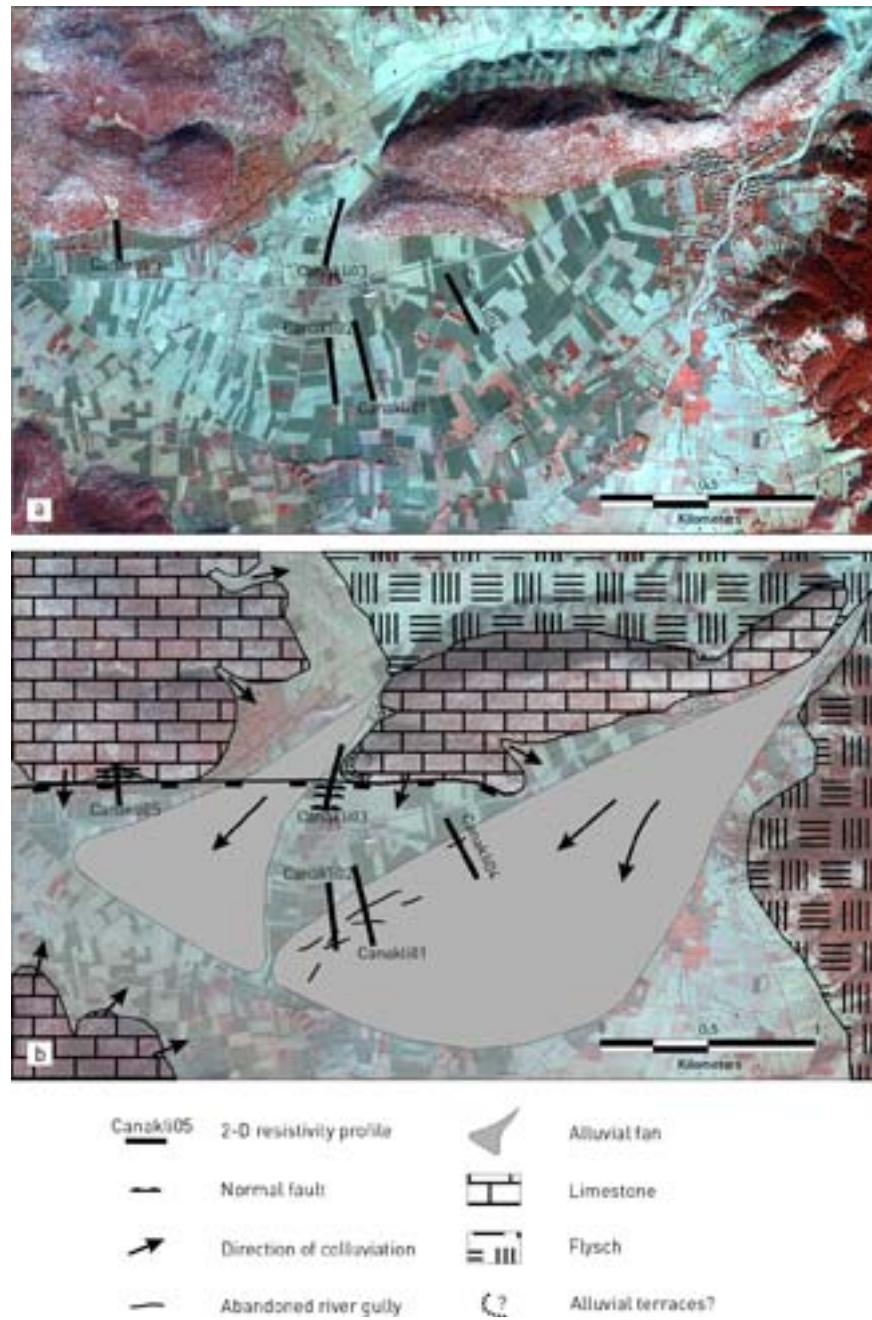
149

Figure 21: Active faulting in the Çanaklı basin as inferred from the 2D-resistivity imagery. (a) Ikonos image with a combination of bands near-infrared, green and blue. See figure 2 for location. (b) Interpretation. Compare to original working hypothesis in figure 6.

7. DISCUSSION AND CONCLUSIONS

Remote sensing analysis of the wider area around the Çanaklı basin revealed heavily dissected and hence uplifted sandstones (Burdigalian to Langhian in age) north of the valley, inferring active normal faulting within the area. Moreover, the Çanaklı basin is the southwestern portion of a lineament, interpreted as the Çanaklı-Isparta Çayı fault zone (Similox-Tohon *et al.*, this volume b).

Subsequent research focused on two lineaments, an EW trending lineament (C1), limiting the basin to the north, and an NE-SW trending lineament (C2) within the valley (Figure 21). The latter lineament has no geomorphological expression, apart from some slight colour difference of the soil. Inversion results, moreover, show that this lineament does not show up at all in the profiles. The Çanaklı basin seemingly consists of a very thick (> 45 m) sequence of low-resistivity material, probably Quaternary clays, as evidenced by hand drillings. There is no evidence for any tectonic disturbance.

Field evidence, however, demonstrates that the limestone front, which is the geomorphological expression of the EW trending lineament (C1), bears the characteristics of an Aegean-type normal fault (Hancock and Barka, 1987; Stewart and Hancock, 1988; 1990; 1991). The degradation of the limestone fault scarp, however, hampers to identify conclusive evidence for historical fault activity. Moreover, the time resolution of the available surface material is too poor to enable identifying historical or recent surface-rupturing events. The fault scarp clearly shows up on two of the resistivity profiles as a very sharp and straight, steeply S-dipping contact between high-resistivity material, i.e. the limestone in the footwall, in the north and low-resistivity material in the south, i.e. the clays in the hanging wall of the fault. Taking into account the minimum thickness of the low-resistivity material, a minimum finite displacement of 45 m can be inferred. On a third resistivity profile within the depression, but along strike with respect to the inferred EW trending normal fault, the presence of the fault within the Quaternary deposits can not be proven or excluded due to the small variation in resistivity.

Although this fault bears no evidence of historical or recent activity the overall interpretation of the 2D-resistivity profiles in the Çanaklı basin (Figures 20 and 21) suggests Quaternary fault activity. We, therefore, consider this newly identified fault, the **Çanaklı fault**, as an active fault. The fault scarp is EW trending and has a length of ca. 3 km. The identified active fault has, moreover, an appropriated orientation with respect to the current dominant stress field (Verhaert *et al.*, 2006) to be considered potentially hazardous.

The Çanaklı fault is the second active fault we thus have identified in the territory of Sagalassos, besides the Sagalassos fault (Similox-Tohon *et al.*, 2005; Similox-Tohon *et al.*, 2006; 2007; Similox-Tohon *et al.*, 2004). It is striking that both faults have a very similar orientation, different from the overall NE-SW trend of the majority of active faults within the Fethiye-Burdur fault zone. To date, only the Sagalassos fault bears evidence of historical surface rupturing (Similox-Tohon *et al.*, 2005; Similox-Tohon *et al.*, 2006; Similox-Tohon *et al.*, 2004; Sintubin *et al.*, 2003). Although the Çanaklı fault is only situated 10 km to the south of the ancient city of Sagalassos, there is currently no reason to retain this active fault as a potential candidate for the causative fault for the destructive Sagalassos earthquake(s) during the 6th to 7th century AD (Waelkens *et al.*, 2000). Therefore, the most likely candidate remains the 'Sagalassos fault' itself.

8. ACKNOWLEDGMENTS

9. REFERENCES

BARKA, A.A., REILINGER, R., SAROGLU, F. and SENGÖR, A.M.C. (1995) The Isparta Angle: Its importance in the neotectonics of the Eastern Mediterranean Region, *International Earth Sciences Colloqium on the Aegean Region* 1: 3-17.

BOZKURT, E. (2001) Neotectonics of Turkey – a synthesis, *Geodinamica Acta* 14: 3-30.

BURBANK, D.W. and ANDERSON, R.S. (2001) *Tectonic Geomorphology*, Blackwell Science, Malden, Massachusetts.

CAMELBEECK, T. and MEGHRAOUI, M. (1998) Geological and geophysical evidence for large palaeo-earthquakes with surface faulting in the Roer Graben (northwest Europe), *Geophysical Journal International* 132: 347-362.

CAPUTO, R., HELLY, B., PAVLIDES, S.B. and PAPADOPOULOS, G.A. (2004) Palaeoseismological investigation of the Tyrnavos Fault (Thessaly, Central Greece), *Tectonophysics* 394: 1-20.

CAPUTO, R., PSCITELLI, S., OLIVETO, A., RIZZO, E. and LAPENNA, V. (2003) The use of electrical resistivity tomographies in active tectonics: examples from the Tyrnavos Basin, Greece, *Journal of Geodynamics* 36: 19-35.

DEGRYSE, P., MUCHEZ, P., SINTUBIN, M., CLIJSTERS, A., VIAENE, W., DEDEREN, M., SCHROOTEN, P. and WAELKENS, M. (this volume). Geological mapping of the area around Sagalassos (SW Turkey), In: P. DEGRYSE and M. WAELKENS (eds.) *Sagalassos VI. Geo- and Bio-Archaeology at Sagalassos and in its Territory*, Leuven University Press, Leuven: 17-24.

EYIDOĞAN, H. and BARKA, A.A. (1996) The 1 October 1995 Dinar earthquake, SW Turkey, *Terra Nova* 8: 479-485.

HANCOCK, P.L. and BARKA, A.A. (1987) Kinematic indicators on active normal faults in western Turkey, *Journal of Structural Geology* 9(5/6): 573-584.

LOKE, M.H., ACWORTH, I. and DAHLIN, T. (2001) A comparison of smooth and blocky inversion methods in 2-D electrical imaging surveys, *ASEG 15th Geophysical Conference and Exhibition*, Brisbane: 4.

LOKE, M.H. and BARKER, R.D. (1996) Practical techniques for 3-D resistivity surveys and data inversion, *Geophysical Prospecting* 44: 499-523.

PAVLIDES, S.B. and CAPUTO, R. (2004) Magnitude versus faults' surface parameters: quantitative relationships from the Aegean Region, *Tectonophysics* 380: 159-188.

PRICE, S.P. and SCOTT, B. (1991) Pliocene Burdur basin, SW Turkey: tectonics, seismicity and sedimentation, *Journal of the Geological Society, London* 148: 345-354.

SENEL, M. (1997a) *1:100 000 geological map of the Isparta – J11 Quadrangle,* General Directorate of Mineral Research and Exploration, Ankara.

SENEL, M. (1997b) *1:250 000 geological maps of Turkey – Isparta No. 4*, General Directorate of Mineral Research and Exploration, Ankara.

SIMILOX-TOHON, D., FERNANDEZ-ALONSO, M., WAELKENS, M., MUCHEZ, P. and SINTUBIN, M. (this volume a) Testing diagnostic geomorphological criteria of active normal faults in the Burdur-Isparta region (SW Turkey), In: P. DEGRYSE and M. WAELKENS (eds.) *Sagalassos VI. Geo- and Bio-Archaeology at Sagalassos and in its Territory*, Leuven University Press, Leuven: 53-74.

SIMILOX-TOHON, D., FERNANDEZ-ALONSO, M., VANNESTE, K., WAELKENS, M., MUCHEZ, P. and SINTUBIN, M. (this volume b) Identifying active normal faults in the Burdur-Isparta region (SW Turkey): remote sensing, surface geology and near-surface geophysics, In: P. DEGRYSE and M. WAELKENS (eds.) *Sagalassos VI. Geo- and Bio-Archaeology at Sagalassos and in its Territory*, Leuven University Press, Leuven: 75-130.

SIMILOX-TOHON, D., SINTUBIN, M., MUCHEZ, P., VANHAVER-BEKE, H., VERHAERT, G. and WAELKENS, M. (2005) Iden-

tification of a historical morphogenic earthquake through trenching at ancient Sagalassos (SW Turkey), *Journal of Geodynamics* 40: 279-293.

SIMILOX-TOHON, D., SINTUBIN, M., MUCHEZ, P., VERHAERT, G., VANNESTE, K., FERNANDEZ-ALONSO, M., VANDYCKE, S., VANHAVERBEKE, H. and WAELKENS, M. (2006) The identification of an active fault by a multidisciplinary study at the archaeological site of Sagalassos (SW Turkey), *Tectonophysics* 420: 371-387.

SIMILOX-TOHON, D., SINTUBIN, M., MUCHEZ, P., VERHAERT, G., VANNESTE, K., FERNANDEZ-ALONSO, M., VANDYCKE, S., VANHAVERBEKE, H. and WAELKENS, M. (2007) Erratum to "The identification of an active fault by a multidisciplinary study at the archaeological site of Sagalassos (SW Turkey)" [Tectonophysics Volume 420 (2006) 371-387], *Tectonophysics* 435: 55-62.

SIMILOX-TOHON, D., VANNESTE, K., SINTUBIN, M., MUCHEZ, P. and WAELKENS, M. (2004) Two-dimensional Resistivity Imaging: a Tool in Archaeoseismology. An Example from Ancient Sagalassos (Southwest Turkey), *Archaeological Prospection* 11: 1-18.

SINTUBIN, M., MUCHEZ, P., SIMILOX-TOHON, D., VERHAERT, G., PAULISSEN, E. and WAELKENS, M. (2003) Seismic catastrophes at the ancient city of Sagalassos (SW Turkey) and their implications for the seismotectonics in the Burdur-Isparta area, *Geological Journal* 38: 359-374.

SINTUBIN, M., SIMILOX-TOHON, D., VERHAERT, G. and MUCHEZ, P. (in prep) New geodynamic model for the region of the lakes (SW Turkey) based on remote sensing, surface geology, archaeoseismology and near-surface geophysics, *Turkish Journal of Earth Sciences.*

SIX, S. (2004) *Holocene Geomorphological Evolution of the Territory of Sagalassos*, Unpublished Ph.D. thesis, Katholieke Universiteit Leuven.

STEWART, I.S. and HANCOCK, P.L. (1988) Normal fault zone evolution and fault scarp degradation in the Aegean region, *Basin Research* 1: 139-153.

STEWART, I.S. and HANCOCK, P.L. (1990) Brecciation and fracturing within neotectonic normal fault zones in the Aegean region. In: R.J. KNIPE and E.H. RUTTER (eds.) *Deformation Mechanisms, Rheology and Tectonics, Specal Publications 54*. Geological Society, London: 105-112.

STEWART, I.S. and HANCOCK, P.L. (1991) Scales of structural heterogeneity within neotectonic normal fault zones in the Aegean region, *Journal of Structural Geology* 13(2): 191-204.

STIROS, S.C. (1996) Identification of Earthquakes from Archaeological Data: Methodology, Criteria and Limitations, In: S.C. STIROS and R.E. JONES (eds.), *Archaeoseismology (Fitch Laboratory Occasional Paper 7)*. Institute of Geology and Mineral Exploration and The British Scholl at Athens, Athens: 129-152.

152

Taymaz, T. and Price, S.P. (1992) The 1971 May 12 Burdur earthquake sequence, SW Turkey: a synthesis of seismological observations, *Geophysical Journal International* 108: 589-603.

ten Veen, J.H. (2004) Extension of Hellenic forearc shear zones in SW Turkey: the Pliocene-quaternary deformation of the Esen Cay Basin, *Journal of Geodynamics* 37(2): 181-204.

ten Veen, J.H. and Kleinspehn, K.L. (2002) Geodynamics along an increasingly curved convergent plate margin: Late Miocene-Pleistocene Rhodes, Greece, *Tectonics* 21(3), 10.1029/2001TC001287.

ten Veen, J.H. and Kleinspehn, K.L. (2003) Incipient continental collision and plate-boundary curvature: Late Pliocene-Holocene transtensional Hellenic forearc, Crete, Greece, *Journal of the Geological Society, London* 160: 161-181.

Vanneste, K., Verbeeck, K., Camelbeeck, T., Paulissen, E., Meghraoui, M., Renardy, F., Jongmans, D. and Frechen, M. (2001) Surface-rupturing history of the Bree fault scarp, Roer Valley graben: Evidence for six events since the late Pleistocene, *Journal of Seismology* 5: 329-359.

Verhaert, G., Similox-Tohon, D., Vandycke, S., Sintubin, M. and Muchez, P. (2006) Different stress states in the Burdur-Isparta region (SW Turkey) since Late Miocene times: a reflection of a transient stress regime, *Journal of Structural Geology* 28: 1067-1083.

Waelkens, M., Sintubin, M., Muchez, P. and Paulissen, E. (2000) Archeological, geomorphological and geological evidence for a major earthquake at Sagalassos (SW Turkey) around the middle of the seventh century AD, In: W.J. McGuire, D.R. Griffiths, P.L. Hancock and I.S. Stewart (eds.) *The Archaeology of Geological Catastrophes* (*Special Publications 171*). Geological Society, London: 373-383.

153